Received: March 7, 2019 Revised: June 27, 2019 Accepted: July 17, 2019

(onlinelibrary.wiley.com) DOI: 10.1111/ner.13031

Comparing Current Steering Technologies for Directional Deep Brain Stimulation Using a Computational Model That Incorporates Heterogeneous Tissue Properties

Simeng Zhang, PhD*; Peter Silburn, PhD†; Nader Pouratian, MD, PhD‡; Binith Cheeran, MD, PhD*; Lalit Venkatesan, PhD*; Alexander Kent, PhD*; Alfons Schnitzler, Dr. Med§

Objective: A computational model that accounts for heterogeneous tissue properties was used to compare multiple independent current control (MICC), multi-stim set (MSS), and concurrent activation (co-activation) current steering technologies utilized in deep brain stimulation (DBS) on volume of tissue activated (VTA) and power consumption.

Methods: A computational model was implemented in Sim4Life v4.0 with the multimodal image-based detailed anatomical (MIDA) model, which accounts for heterogeneous tissue properties. A segmented DBS lead placed in the subthalamic nucleus (STN). Three milliamperes of current (with a 90 μs pseudo-biphasic waveform) was distributed between two electrodes with various current splits. The laterality, directional accuracy, volume, and shape of the VTAs using MICC, MSS and co-activation, and their power consumption were computed and compared.

Results: MICC, MSS, and coactivation resulted in less laterality of steering than single-segment activation. Both MICC and MSS show directional inaccuracy (more pronounced with MSS) during radial current steering. Co-activation showed greater directional accuracy than MICC and MSS at centerline between the two activated electrodes. MSS VTA volume was smaller and more compact with less current spread outside the active electrode plane than MICC VTA. There was no consistent pattern of power drain between MSS and MICC, but electrode co-activation always used less power than either fractionating paradigm.

Conclusion: While current fractionalization technologies can achieve current steering between two segmented electrodes, this study shows that there are important limitations in accuracy and focus of tissue activation when tissue heterogeneity is accounted for.

Keywords: Current steering, DBS, MICC, MSS, VTA

Conflict of Interest: Simeng Zhang, Binith Cheeran, Lalit Venkatesan, and Alexander Kent are employees and receive salary from Abbott. Peter Silburn, Nader Pouratian, and Alfons Schnitzler consult for Abbott and receive compensation for their time. Nader Pouratian also serves as a consultant for Medtronic, Boston Scientific, Second Sight Medical Products and receives grand support from Second Sight Medical Products and BrainLab. Alfons Schnitzler serves as a consultant for Boston Scientific, Teva Neuroscience, UCB, MEDA Pharma, Novartis and Abbvie and received research grants from the German Research Council, BMBF, the German Ministry of Education and Health, and the Helmholtz Association.

INTRODUCTION

Deep brain stimulation (DBS) has been established as an effective therapy for movement disorders such as essential tremor (ET) and Parkinson's disease (PD) over the past decades (1–6). Traditionally, DBS uses 120–185 Hz pulses via a lead implanted in a target brain structure, such as the subthalamic nucleus (STN).

Accurate targeting of the correct brain structure is important for maximizing the clinical benefit of DBS therapy. However, the target structure is often small, non-spherical in shape with complex substructures (7), and surrounded by other structures which upon stimulation can cause adverse side effects (8–10). Generating optimal therapy without triggering side effects can be a major challenge if the lead is not implanted optimally.

Address correspondence to: Simeng Zhang, PhD, Neuromodulation Division, Abbott, 6901 Preston Rd. Plano, TX 75024, USA. Email: david.zhang@abbott.com

* Neuromodulation Division, Abbott, Plano, TX, USA;
† Queensland Brain Institute, The University of Queensland, Brisbane, Australia;
‡ Department of Neurosurgery, University of California Los Angeles, Los Angeles, CA, USA; and
§ Institute of Clinical Neuroscience and Medical Psychology and Department of Neurology, Heinrich Heine University, Düsseldorf, Germany

For more information on author guidelines, an explanation of our peer review process, and conflict of interest informed consent policies, please go to www.wiley.com/WileyCDA/Section/id-301854.html

Source(s) of financial support: This study is funded and supported by Abbott.

A recent technological development in DBS is leads with radially segmented electrodes. Modeling studies (11–13) and preclinical studies (14) have shown that stimulation through a segmented electrode allows for steering current axially toward the therapy target, while avoiding regions that produce side effects. Pilot studies using segmented DBS leads have demonstrated the ability to improve outcomes by allowing clinicians to customize and shape stimulation to individual patient's anatomy (15,16).

For segmented lead systems, using only a single activated electrode (known as single-segment activation or SSA) is often sufficient to produce customized axially asymmetric directional fields (15,17–19), but in some cases where a higher level of customizability of the activated tissue is desired, current fractionalization techniques can be used. Current fractionalization is defined as distributing currents through two or more electrodes. While allowing for high level of user control of the activated tissue, current fractionalization also increases the complexity of programming (20) and may reduce the implantable pulse generator (IPG) lifespan.

To date, two current fractionalization approaches are available for clinical use. The first approach is multi-stim set (MSS), or sometimes called "interleaving," which rapidly alternates multiple stimulation sets that can have different stimulation parameters, apart from a shared stimulation frequency (Fig. 1a). Systems with a single current source employ MSS to enable current fractionalization. The second approach is multiple independent current control (MICC), which is implemented by capping the total amount of current and distributing portions of the total current independently through two or more electrodes (Fig. 1b). Some systems offer concurrent activation of multiple electrodes via parallel hardware connection (enabling the combination to be treated as a single electrode), or "coactivation" (Fig. 1c). Coactivation can decrease the overall impedance of the electrodes, therefore may result in less power utilization in current-controlled systems but may also produce a volume of tissue activation (VTA) whose directionality can vary based on interelectrode impedance (15). Therefore, coactivation is considered a limited current fractionalization technique.

This study used computational models to compare the performance and power consumption of MICC, MSS, and coactivation by comparing the volume of tissue activated (VTA). A significant limitation of prior studies of VTA modeling of current fractionalization methodologies has been the use of homogenous tissue models. In order to allow for a more accurate study of interelectrode field steering, we used the multimodal image-based detailed anatomical (MIDA) model (21), which contains detailed representations of numerous structures surrounding the DBS lead, brain nuclei, white matters, blood vessels, bones and skull layers, brain surfaces, meninges, cerebrospinal fluids, and soft tissues inside of a human head, and the IT'IS database 3.1.1 (22), which assigns inhomogeneous tissue properties to all of the MIDA structures. As a result, the calculation of VTAs is more accurate (23–27) than using simple homogeneous models used previously (28). We focused on testing the effects of current fractionalization (via various current splits, see methods) between electrodes on VTA laterality, directional accuracy, volume, shape, and power drain for each paradigm.

METHODS

A finite element model (FEM) of the human head (Supplementary Fig. 1a) was implemented in Sim4Life v4.0 with the MIDA model (21). A segmented DBS lead (cylindrical electrode at the top and bottom of the array, and two tri-trodes in-between- a 1–3–3-1 design) with 0.5 mm interelectrode spacing was placed in the STN, with the lead tip positioned near the ventral STN border, and a 0.5-mm thick encapsulation layer (29) was added around the lead. The electrical conductivity and relative permittivity of the brain tissues, platinum-iridium contacts on the DBS lead, and polyurethane insulation on the lead were determined from the IT'IS database 3.1.1 (22). Electrical potentials were calculated using various contact configurations by setting the boundaries of the active contacts to a voltage-controlled condition (Dirichlet boundary condition). The return electrode (anode) of the monopolar stimulation was represented using the boundaries of the epidermis layer in the MIDA head model. A bounding box of size 175.2 × 227.5 × 251.5 mm that encompassed all other model structures was modeled with zero normal current density (Neumann boundary condition). To determine the equivalent current delivered, the total current flux was calculated over the boundary of the cathode(s). Given the input voltage and the current flux on the cathode(s), an impedance of the electrode-tissue interface (ETI) was calculated and the equivalent current delivered was computed.

A rectilinear, volumetric mesh grid was generated from the model geometries with 0.1 mm maximum step size for the electrode and structures near the electrode, and 2.5 mm maximum step size elsewhere (over 101 million elements total). Convergence was set to a relative value of 1×10^{-8} and an absolute value of 1×10^{-10}. Finally, an electromagnetic ohmic quasi-static solver was used to solve the

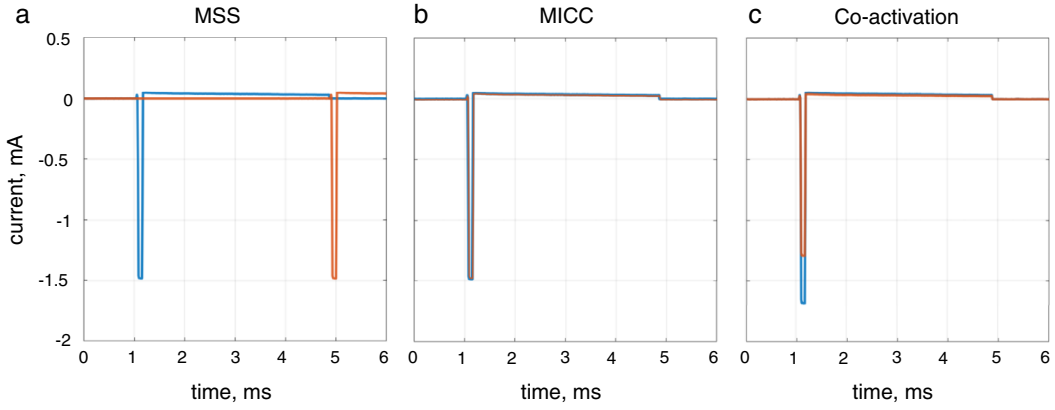

Figure 1. a. MSS pulses at 1.5 mA each. The second pulse arrives at the 50% phase offset from the first pulse. b. MICC pulses at 1.5 mA each, the two pulses arrive at the same time. c. Coactivation pulses at 3 mA total. The two pulses arrive at the same time, but the amplitudes of the pulses are determined by the interelectrode impedances. [Color figure can be viewed at wileyonlinelibrary.com]

following equation at the mesh nodes at the given current amplitude and frequency:

$$\nabla \cdot \bar{\epsilon} \nabla \varphi = 0 \quad (1)$$

where $\bar{\epsilon}$ is the complex electric permittivity, ϕ is the electric potential, and:

$$\bar{\epsilon} = \epsilon_R \epsilon_0 + \frac{\sigma}{j\omega} \quad (2)$$

where ϵ_R is the relative permittivity, ϵ_0 is the relative permittivity of perfect vacuum, and σ is the electrical conductivity.

Multicompartment axons (30) of 10 mm length and 5.7 μm diameter were distributed on planes of 1 mm spacing that were perpendicular to the lead. Within each plane, the axons were arranged parallel to one another with 0.25 mm spacing and rotated 5 times by 30 degrees per rotation (Supplementary Fig. 1c). The electrical potentials from the FEM (Supplementary Fig. 1b) were interpolated along each neuron and delivered as an extracellular stimulation to determine which axons were activated for a given contact configuration and stimulation set. The VTA was then calculated by linking the sites of first action potential initiation within the axon grid (11,24). All neuronal activations were computed in Sim4Life.

A total of 3 mA of current was distributed between two electrodes in the same row (2B|2A) or along the same column (2B|3B, or 2ABC|ABC in ring modes). In this study, electrode 2B was chosen as the base electrode because it faced posterior-lateral STN, a region demonstrated to offer the most therapeutic effect when stimulated (31,32). The current splits between the two electrodes extended from 100%–0%, 87.5%–12.5%, 75%–25%, 62.5%–37.5%, 50%–50% … 0%–100% for the computational experiments with electrodes 2B and 2A, respectively, and from 100%–0% to 50%–50% following the same 12.5% step resolution for the computational experiments with electrodes 2B|3B and 2ABC|3ABC. A pseudo-biphasic waveform (recorded from the DBS contacts in saline) with 90 μs pulse width was delivered at 130 Hz. For the MICC paradigm, the two pulses were delivered simultaneously, and for MSS paradigm, the second pulse was introduced at a 50% phase offset from the first pulse.

Four classes of measures were used to classify the VTA: laterality (radial distance of displacement vectors), directional accuracy (angle of the displacement vectors), volume (volume, spread), and shape (mean differential radius). In addition, power consumption was also calculated for each current steering paradigm.

The *laterality* and *directional accuracy* of the VTA was quantified by analyzing the centroid of the boundaries on each axonal plane. The *displacement vectors* were defined as vectors pointing from the center of the DBS lead to the centroid of the VTA boundary on each axonal plane in polar coordinates (Fig. 2a). From the displacement vectors, the radial distance and angle can be used to quantify the laterality and directional accuracy of the VTA from the center of the DBS lead.

The *volume* of the VTA was calculated by finding the polygon that was bounded by sites of the first initiated action potential after each pulse in each axonal plane, and calculating the volume enclosed by the bounding polygon stacks. The action potential sites that were more than three standard deviations away from the population on each plane were considered outliers and were not included for VTA calculation. For MSS, the two volumes elicited by two sequential pulses were summated to produce a single volume. We also performed a single calculation of VTA volume when coactivating 2B and 2A by assigning the 3 mA of equivalent currents of 2B and 2A according to their impedance when shorted together. The *spread* of the VTA was calculated by dividing the volume of a given VTA by the VTA generated by activating only electrode 2B (or electrode 2ABC in ring mode) at 3 mA (100%–0% current split). This measure reflects the percentage of volume change relative to an SSA.

The shape measure *mean differential radius* was defined as the average of the linear distances between points on MICC boundaries and their closest point on the MSS boundaries on each axonal plane. This measure compares the VTA of MICC and MSS on each axonal plane. The power consumption (represented using battery draw current) of the MICC, MSS, and coactivation (CoA) paradigms were calculated using the following sets of equations:

$$I_{\mathrm{MICC}} = I_{\mathrm{overhead}}(f) + (I_{E1} + I_{E2}) * PW * f * \frac{V_{\max}}{V_{\mathrm{bat}}} \quad (3)$$

$$I_{\mathrm{MSS}} = I_{\mathrm{overhead}}(2*f) + I_{E1} * PW * f * \frac{V_{E1}}{V_{\mathrm{bat}}} + I_{E2} * PW * f * \frac{V_{E2}}{V_{\mathrm{bat}}} \quad (4)$$

$$I_{\mathrm{CoA}} = I_{\mathrm{overhead}}(f) + 2*\mathrm{I} * PW * f * \frac{V_{eq}}{V_{\mathrm{bat}}} \quad (5)$$

where I_{overhead} is the frequency-dependent overhead current from the IPG circuit, f is the stimulation frequency, I_{E1} and I_{E2} are the stimulation current amplitude for electrodes 1 and 2, PW is the pulse width, V_{E1} and V_{E2} are the load voltages for electrodes 1 and 2 according to their respective ETI impedances, $V_{\max}$ is the load voltage with maximum impedance between the two electrodes, V_{eq} is the load voltage for the shorted electrodes with their equivalent impedance, and finally, V_{bat} is the battery voltage.

RESULTS

Impedance

This work compared VTAs generated with MSS and MICC paradigms as a fixed total current is progressively fractionated between two electrodes (or sets of electrodes). In a current-controlled DBS system, the size of the VTA is influenced by the impedance of the ETI. Therefore, we calculated the impedance values of all ETIs by dividing the input voltage by the current through the cathodes from the FEM. The impedance of the ETI at electrode 2B, 2A, 3B, 2ABC, and 3ABC were calculated to be 1.147, 1.496, 1.337, 0.590, and 0.693 kΩ, respectively. In the case of coactivation, parallel connection of 2B and 2A resulted in an equivalent electrode impedance of 0.649 kΩ.

VTA Laterality

Laterality of the VTA was measured by the radial distance of the displacement vectors. Figure 2b summarized displacement vectors of all current splits in polar coordinates for axonal planes 1, 3, and 7. Plane 1 and 7 were the bottom and top planes, indicating the planes most proximal and distal to the lead tip. Plane 3 was where electrodes 2B and 2A were centered on, denoted as the "electrode plane." As the current split shifted from 100%–0% (SSA) to 50%–50%, the radial distance decreased, indicating that the volume was pulled toward the center of the lead. In addition, radial distances did not show substantial differences between the MICC and MSS on the electrode plane, but MSS exhibited overall smaller radial distances on the top and bottom planes. The displacement vectors for the VTA obtained by coactivation of electrodes 2B and 2A were also plotted (Fig. 2b, green squares) for

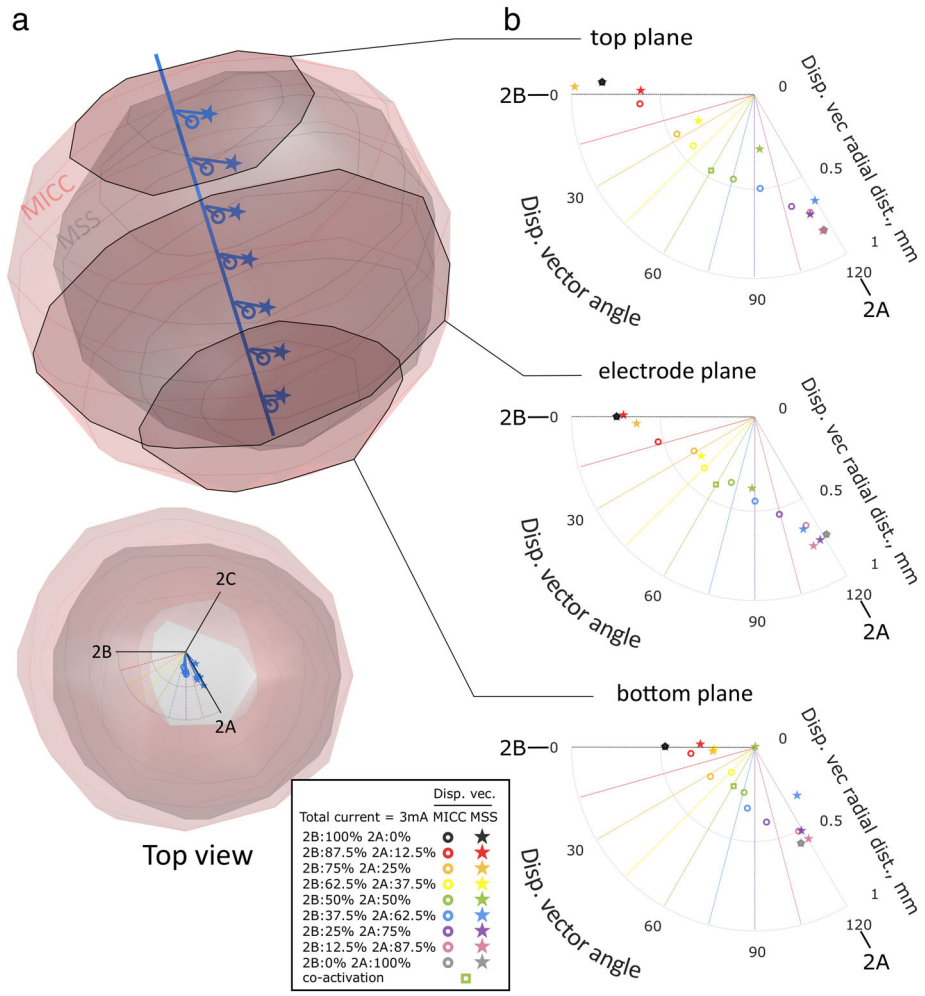

Figure 2. a. An example (37.5%–62.5% split) of the 3D representation of displacement vectors (oblique and top view) on each axonal plane with MICC (red) and MSS (black) VTAs, shaded planes show the top, bottom, and electrode planes. b. Displacement vectors of the VTAs for all current splits on the top, bottom, and electrode planes, also showing displacement vectors of the coactivation VTA. Radial guidelines indicate the perfect current steering angles for all current splits. [Color figure can be viewed at wileyonlinelibrary.com]

comparison. The coactivation VTA displacement vectors had a similar radial distance as MICC at 50%–50% current split (Fig. 2b, green stars) at all three planes.

VTA Directional Accuracy

The angle of the displacement vectors reflects the directional accuracy of current steering. In a "perfect" current steering scenario, the displacement vectors are expected to shift every 15 degrees for the nine current split conditions (radial guidelines in Fig. 2b, Fig. 3b). In this case, the displacement vector angles for MICC, MSS, and coactivation were found to be generally consistent across axonal planes at each current split (Supplementary Video). Therefore, an average angle of the displacement vectors could be obtained by averaging across axonal planes at each current split (seen in Fig. 3b). Overall, MICC showed a relatively higher performance in directional accuracy, with the maximum deviation of 14.8 degrees from the "perfect" steering angle (occurred at 37.5%–62.5% current split). MSS showed more pronounced directional inaccuracy than MICC, with the maximum deviation of 43.3 degrees from the "perfect" steering angle (also occurred at 37.5%–62.5% current split). Both the MICC and MSS paradigms showed an overshoot then lag of directional accuracy in directional steering. This will be further discussed in the Discussion section. The displacement vectors for coactivation had a 60-deg angle at the electrode plane (green squares in Fig. 2b), and clustered close to 60 degrees at all other axonal planes (Supplementary Video), which indicated that directional accuracy for coactivation was close to being "perfect."

VTA Volume and Spread

In the modeling experiment with electrode 2B|2A, the MSS VTA volume in response to various current splits was nonlinear and was 40% smaller (at 50%–50% current split) than the VTA obtained by coactivation of electrodes 2B and 2A (Fig. 3a). MICC VTA had a linear response to current split (due to the impedance mismatch, see Discussion section) but was as much as 36.6% larger (at 50%–50% current split) compared to the corresponding MSS VTA and 11.2% larger than coactivation. The impacts are better understood in conjunction with the shape analysis.

The MSS VTA exhibited an average spread of 0.86, whereas MICC had an average spread of 1.17 (averaged for all except 100%–0% and 0%–100% current split), which demonstrated that splitting currents between two electrodes caused a decrease of

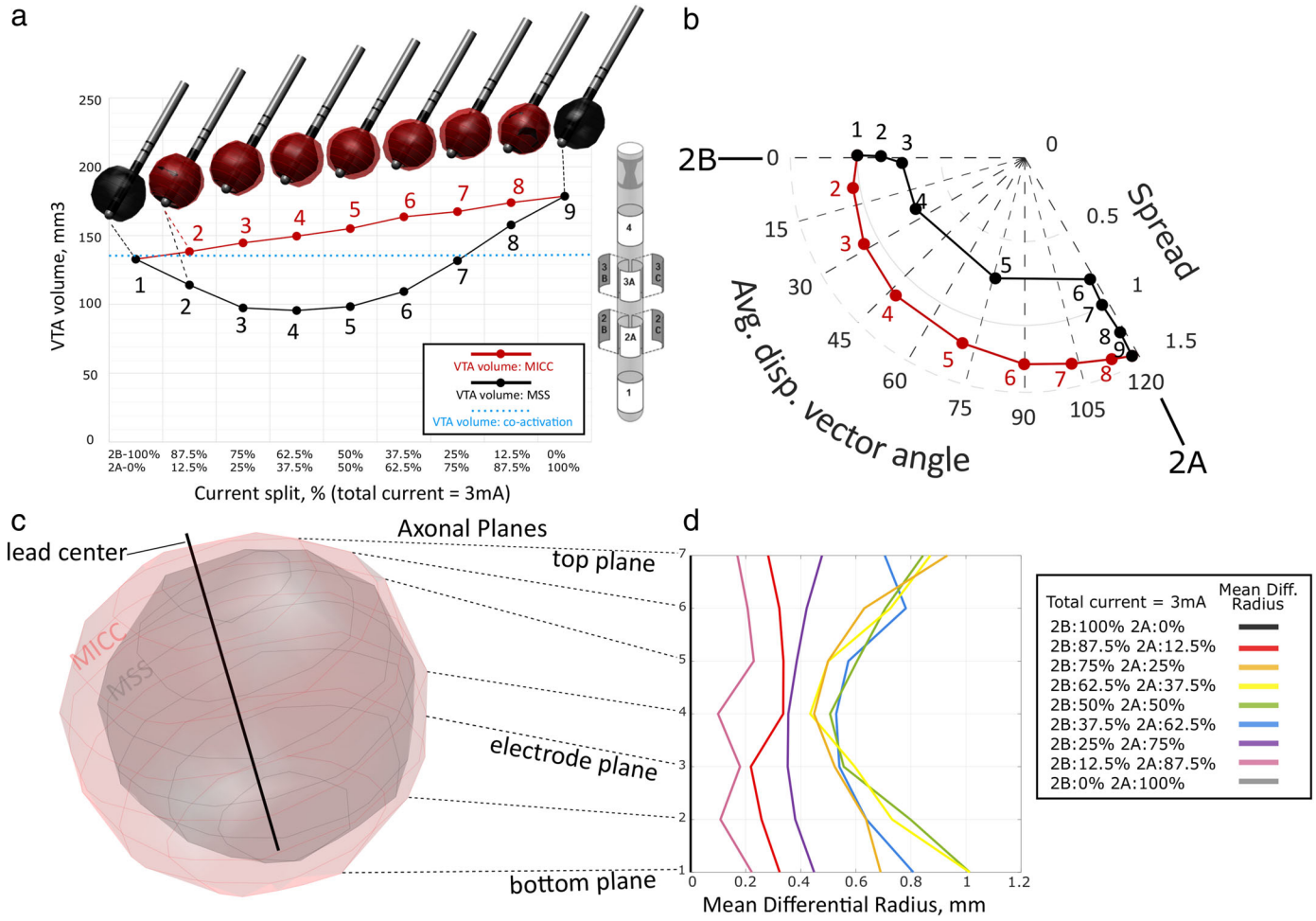

Figure 3. a. VTA volumes of MICC and MSS paradigms for various current (coactivation VTA is also shown). Numbers near the data points were used to denote the sequence of the current splits. b. The spread of VTA for MICC and MSS paradigms in polar coordinates with respect to average displacement vector angles. Dashed radial guidelines indicate the perfect current steering angles for all current splits. c. An example of the MICC (red) and MSS (black) VTAs, showing all axonal planes. d. Mean differential radius along the axonal planes. Axonal plane 1 is the bottom plane (most proximal to the lead tip) and 7 is the top plane. [Color figure can be viewed at wileyonlinelibrary.com]

volume for MSS and an increase of volume for MICC compared to an SSA (Fig. 3b).

VTA Shape

Since the MICC VTA generally encompassed the respective MSS volume (Fig. 3c), the mean differential radius generally remained positive. As the current split shifted from 100%–0% to 50%–50%, the mean differential radius showed more discrepancy, particularly at the top and bottom axonal plane (most distal and proximal planes along the lead axis), forming a more "parabolic" profile along the length of the lead (Fig. 3d). The maximum mean differential radius was found at the 50%–50% current split on axonal plane 1 (most distal end of the DBS lead), where the MICC boundary extended an average of 1 mm further than the MSS boundary.

Vertical Steering

In the "vertical" current steering experiment with electrode 2B and 3B, or ring mode with electrodes 2ABC and 3ABC, the volume (and spread) exhibited similar trends as those of 2B and 2A (Fig. 4a). Instead of winding around the circumference of the lead with changes in current split, the VTA spread across the length of the lead (Fig. 4b). The displacement vector across all axonal planes were shown in Figure 4c. The displacement vectors for the ring mode, expectedly, aggregated at the center of the lead due to a symmetrical activation. Similarly, the displacement vectors for 2B and 3B aggregated at the direction of the electrodes 2B and 3B and did not show any radial shift. The mean differential radius was shown in Figure 4d. Between the experiment of 2B|3B and 2ABC|3ABC, the mean differential radius showed similar trend. Axonal plane 1 exhibited the least amount of differences between MICC and MSS VTA while axonal plane 5–8 generally exhibited the most amount of differences.

Power

Lastly, the results of the power consumption calculation indicated that the battery current draw for either fractionalization paradigm (MICC or MSS) is highly dependent on the impedance of the ETI and input current, and that coactivation always results in a lower battery draw than fractionalization. We created three parameter sets to demonstrate the complexity of these dependencies:

1. The parameters were the same as our previously simulations, where electrode 2B and 2A had respective impedances of

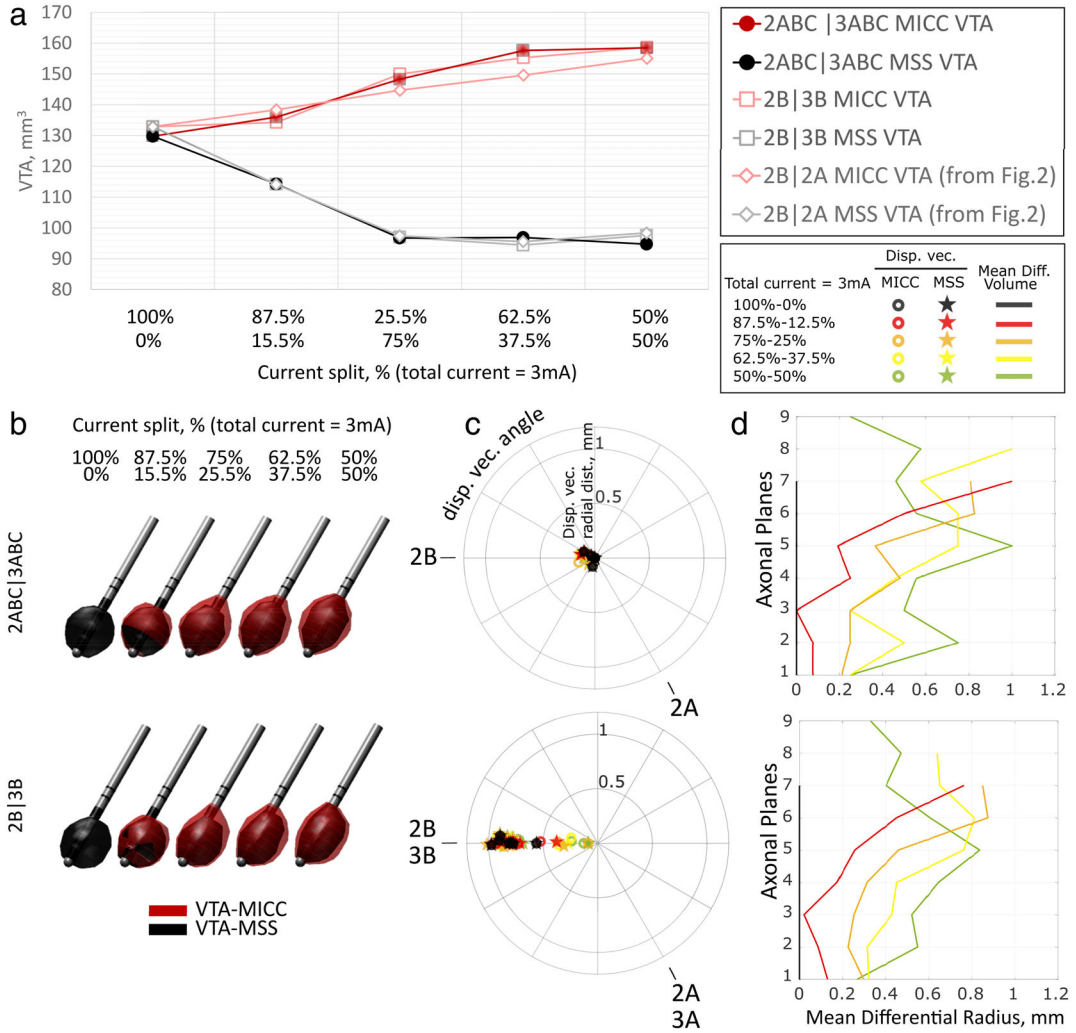

Figure 4. a. VTA volumes for single-segment versus ring mode activations for MICC and MSS conditions. b.-d. Rendered volumes, displacement vectors, and mean differential radius of VTAs for ring mode activation (2ABC|3ABC) and single-segment activation (2B|3B). [Color figure can be viewed at wileyonlinelibrary.com]

1.147 and 1.496 kΩ, and received 1.5 mA of current each. In this situation, MSS current drew 40% more current than MICC, while coactivation drew 7.8% less current than MICC.

2. A scenario presented by Schüpbach et al (28) where the two electrodes have an unmatched impedance of 1.5 and 3 kΩ. For the case in which the two electrodes were each passed 2 mA of current, MSS drew 2.1% less current than MICC, while coactivation drew 27.9% less current than MICC.
3. In a more extreme scenario where the two electrodes have the same impedance as stated by reference [(2)], but the electrode with the higher impedance received 3 mA while the other received 2 mA, MSS drew 13.3% less current than MICC, while coactivation drew 29.7% less current than MICC.

DISCUSSION

VTA modeling has furthered our understanding of the impacts of different electrode montages on tissue activation. VTA visualizations of the effects of current steering with directional DBS systems and interelectrode current fractionalization techniques show nearly limitless ability to accurately focus and steer the VTA, leading some to propose VTA-based visually guided programming of DBS systems.

However, the models utilized by visually guided programming software did not account for any degree of tissue heterogeneity. Recent studies have shown the vital importance of tissue inhomogeneity (23) and even the heterogeneity of the soft tissues (26) on computational modeling results. Prior publications also studied the effects of impedance on current steering with MICC in the case of a perfect impedance-matched scenario (33), and at extremes of impedance-mismatch (28). In this study, we modeled the ETI with real-life scenarios in a widely accepted heterogeneous brain tissue model and accounted for a clinically relevant interelectrode impedance (27%), hence the modeling in this study is proposed to be more relevant in understanding how the VTA volumes spread as current fractionalizes.

In this study, we used VTA *laterality*, *directional accuracy*, *volume*, *shape*, *and power* measures to study the VTA produced with three current-controlled current fractionalization methods, MICC, MSS, and coactivation.

The *laterality and directional accuracy* of the VTAs were quantified using displacement vectors, which contains two measures, radial distance and angle, corresponding to the laterality and

directional accuracy of the VTA volume on every axonal plane (Fig. 2b, full sets of displacement vectors for all axonal planes could be found in Supplementary Video). Firstly, radial distance did not show substantial differences between the MICC and MSS on the electrode plane, while MSS observed smaller radial distances at the top and bottom planes. This implies that the MSS could produce VTA of more focus on the electrode plane with less volume spreading onto other planes. In addition, both MICC and MSS produced less VTA radial distance than SSA. This is consistent with previous studies that demonstrated the SSA produces VTAs with the most laterality (15).

Secondly, MSS showed a larger discrepancy in directional accuracy, but both MICC and MSS showed discrepancy, nonetheless. This indicates that to achieve perfect current steering, using prefractionalized current splits alone with MICC is not sufficient, as minor adjustments on current splits are needed. This is especially well illustrated in the MSS paradigm, where radial steering did not initiate until the 62.5%–37.5% current split and aggregated toward the other electrode after the 37.5%–62.5% current split. This implies that to achieve perfect steering of 15 degrees at every current split, MSS will require even finer resolution adjustment of current splits than MICC. However, this delay and then overshoot of the MSS VTA steering was not observed in activation of electrodes along the DBS lead (vertical steering), such as 2B and 3B (Fig. 4b). Note that in this study, "perfect" steering angles was only represented as a measurement for the implementation of visually guided programming. The clinical relevance of "perfect steering" is not yet clear as a "sufficient steering" has not yet been clearly established (i.e., clinically sufficient to reduce off target side effects with minimal programming burden).

Under certain conditions, coactivation demonstrated advantages in VTA steering accuracy compared to the other fractionalization methods. It is also worth noting that, in this model, with less than 27% interelectrode impedance difference (electrodes 2B and 2A at 1.147 and 1.496 kΩ respectively), the angle of the displacement vectors for electrode co-activation lies at the "perfect" steering axis of 60 degrees (Fig. 2b, Supplementary Video), outperforming MSS and MICC in radial current steering accuracy. If the interelectrode impedance difference is at the extreme end of that seen physiologically (100% variation in adjacent segments) as discussed in Schüpbach et al (28), the angle of the steering would be off the perfect steering axis in a homogeneous tissue model. Overall, this implies that coactivation can provide greater focus and better steering accuracy when interelectrode impedances are within typical physiological parameter.

Overall, for a given set of parameters, both current fractionalization techniques showed changes in VTA *volume* as the current split shifted from 100%–0% to a 50%–50% distribution. In an MICC DBS system, the VTA volume has a linear relationship with the impedance, which resulted in a linear increase in the spread from electrode 2B (lower impedance) to 2A (higher impedance) across current splits in MICC. In the case of MSS, this change was nonlinear, where the smallest volume was observed at current splits 62.5%–37.5%, but in a perfect impedance-matched scenario, the smallest volume would be expected to occur at current splits 50%–50%.

The *shape* difference of VTAs produced by MICC and MSS was better understood by comparing slice-by-slice mean differential radius. In the experiment of electrodes 2B and 2A, as currents split from 100%–0% to 50%–50%, the mean differential radius (Fig. 3d) exhibited a "parabolic" shape that was smaller at the center of the VTA volume and larger at the ends. This indicated that at

Table 1. Summary of Comparison of Various Current Steering Techniques.

	Laterality	Directional accuracy	VTA volume and shape	Power consumption
MICC	Less than SSA when using more than one electrode in the same row	Deviations from expected direction when accounting for heterogeneity	Larger volume, more spread outside the active electrode plane	Depends on the impedance of the ETI
MSS	Less than SSA when using more than one electrode in the same row	More deviations from expected direction than MICC	Smaller volume, more focused at the active electrode plane	Depends on the impedance of the ETI
Coactivation	Less than SSA	Only one direction, but at expected direction with typical interelectrode impedance differences	Smaller volume than MICC, larger than MSS at 50%–50% current split	Lowest due to lowest impedance of ETI

certain current splits, the MSS paradigm minimized VTA activation at the two ends of the VTA, concentrating the activation near the site of the active electrode. In the experiments of electrodes 2B and 3B, as well as 2ABC and 3ABC, because the VTA moved along the length of the DBS lead, the "parabolic" shape was not observed. Instead, the largest mean differential radius usually resided at the top axonal planes (Fig. 4d). This is attributed to the second pulse in the MSS paradigm. A weaker second pulse with MSS produced a smaller volume than a synergistic MICC paradigm, therefore providing more focus of stimulation for the former.

The laterality, directional accuracy, volume, and shape measures of the VTAs demonstrated that the clinical effects of steering through interelectrode current fractionalization may have to incorporate all four measures. Therefore, when using current fractionalization techniques, the clinician may thereby need to titrate amplitude of stimulation in addition to the current fractionalization (current splits), imposing further steps in optimizing clinical programming.

The power calculations showed that MSS, with different sets of parameters, could draw more or less battery current than MICC depending on the ETIs of the electrodes and the input current, while coactivation consistently drew less battery current than fractionalization (MICC or MSS). The increased energy cost for MSS stemmed from the overhead current, as the two interleaved pulses need to be switched on and off, effectively doubling the stimulation frequency. With further technology development, the overhead battery drain could be further minimized to increase the efficiency of MSS.

One limitation of the current study is that a DBS waveform was used that was recorded in saline (to mimic the properties of homogeneous neural tissues) for all modeling. Though this waveform did not account for tissue heterogeneity, it is sufficient to incorporate the capacitive and resistive effect of the electrode metal and a homogeneous ETI on the input waveform. Another limitation of the current study is that we only examined the spatial activation of the MICC and MSS paradigms. The temporal dynamics of the basal ganglia network was not considered. Studies have demonstrated that desynchronized stimulations could provide better therapeutic effects (34,35). MSS could potentially generate similar desynchronization effects, and further research is warranted on its potential benefits.

Finally, because the pulses were individually administered in the MSS paradigm, the second pulse could be switched to a wider (or narrower) pulse width, or a potentially different waveform, and the delay from the first pulse could be changed. In addition to VTA, pathway activations can also be examined. For example, the internal capsule, a pathway near the STN that could cause adverse side effects such as tetanic motor contractions (24) and worsening of other motor symptoms (36) upon stimulation. We plan to incorporate these factors into future modeling work (Supplementary Fig. 1d).

In conclusion, in a clinical setting, for directionally segmented DBS systems, a clinician can choose to use either MSS, MICC, or coactivation to achieve interelectrode current steering with various tradeoffs (Table 1). MSS needs finer current splits to achieve precise radial steering, and MICC needs titration of current amplitude to achieve more focused activation at the active electrode. In cases where current steering was implemented on two vertical electrodes, MSS and MICC are directly comparable. If a clinician wants to achieve the furthest laterality in VTA activation, SSA is more desirable than either MSS or MICC. Last but not least, coactivation may outperform MICC or MSS in precision of steering directionality at certain interelectrode impedance differences and with less power consumption than both MICC and MSS.

Acknowledgement

We like to thank Daran DeShazo, David Schafer and Steve Boor for performing the energy consumption experiment and calculations. This study was sponsored by Abbott.

Authorship Statement

Simeng Zhang, Nader Pouratian, Binith Cheeran, Lalit Venkatesan, Alexander Kent and Alfons Schnitzler were responsible for the conception and design of study. Simeng Zhang was responsible for the acquisition of data. Simeng Zhang, Peter Silburn, Nader Pouratian, Binith Cheeran, Lalit Venkatesan, Alexander Kent and Alfons Schnitzler were responsible for the analysis and/or interpretation of data. Simeng Zhang drafted the manuscript. All authors revised the manuscript critically for important intellectual content. All authors approved the version of the manuscript to be published.

How to Cite this Article:

Zhang S., Silburn P., Pouratian N., Cheeran B., Venkatesan L., Kent A., Schnitzler A. 2020. Comparing Current Steering Technologies for Directional Deep Brain Stimulation Using a Computational Model That Incorporates Heterogeneous Tissue Properties.
Neuromodulation 2020; 23: 469–477

REFERENCES

1. Mansouri A, Taslimi S, Badhiwala JH et al. Deep brain stimulation for Parkinson's disease: meta-analysis of results of randomized trials at varying lengths of follow-up. *J Neurosurg* 2018;128:1199–1213. https://doi.org/10.3171/2016.11.JNS16715.
2. Benabid AL, Pollak P, Louveau A, Henry S, de Rougemont J. Combined (thalamotomy and stimulation) stereotactic surgery of the VIM thalamic nucleus for bilateral Parkinson disease. *Stereotact Funct Neurosurg* 1987;50:344–346. https://doi.org/10.1159/000100803.
3. Deep Brain Stimulation (DBS) for the Suppression of Tremor—Full Text View—ClinicalTrials.gov. https://clinicaltrials.gov/ct2/show/NCT02087046.
4. Clinical Evaluation of the Infinity DBS System—Full Text View—ClinicalTrials.gov. https://clinicaltrials.gov/ct2/show/NCT02989610.
5. Deep Brain Stimulation (DBS) for the Treatment of Parkinson's Disease—Full Text View—ClinicalTrials.gov. https://clinicaltrials.gov/ct2/show/study/NCT01839396.
6. Deep-Brain Stimulation for Parkinson's Disease Study Group, Obeso JA, Olanow CW et al. Deep-brain stimulation of the subthalamic nucleus or the pars interna of the Globus Pallidus in Parkinson's disease. *N Engl J Med* 2001;345: 956–963. https://doi.org/10.1056/NEJMoa000827.
7. Hoover JE, Strick PL. Multiple output channels in the basal ganglia. *Science* 1993; 259:819–821.
8. Moran A, Bergman H, Israel Z, Bar-Gad I. Subthalamic nucleus functional organization revealed by parkinsonian neuronal oscillations and synchrony. *Brain* 2008; 131:3395–3409. https://doi.org/10.1093/brain/awn270.
9. Bevan MD, Magill PJ, Terman D, Bolam JP, Wilson CJ. Move to the rhythm: oscillations in the subthalamic nucleus-external globus pallidus network. *Trends Neurosci* 2002;25:525–531. https://doi.org/10.1016/S0166-2236(02)02235-X.
10. Contarino MF, Bour LJ, Verhagen R et al. Directional steering: a novel approach to deep brain stimulation. *Neurology* 2014;83:1163–1169. https://doi.org/10.1212/WNL.0000000000000823.
11. Butson CR, McIntyre CC. Current steering to control the volume of tissue activated during deep brain stimulation. *Brain Stimul* 2008;1:7–15. https://doi.org/10.1016/j.brs.2007.08.004.
12. Teplitzky BA, Zitella LM, Xiao Y, Johnson MD. Model-based comparison of deep brain stimulation array functionality with varying number of radial electrodes

and machine learning feature sets. *Front Comput Neurosci* 2016;10:58. https://doi.org/10.3389/fncom.2016.00058.
13. Peña E, Zhang S, Deyo S, Xiao Y, Johnson MD. Particle swarm optimization for programming deep brain stimulation arrays. *J Neural Eng* 2017;14:016014. https://doi.org/10.1088/1741-2552/aa52d1.
14. Connolly AT, Vetter RJ, Hetke JF et al. A novel lead design for modulation and sensing of deep brain structures. *IEEE Trans Biomed Eng* 2016;63:148–157. https://doi.org/10.1109/TBME.2015.2492921.
15. Rebelo P, Green AL, Aziz TZ et al. Thalamic directional deep brain stimulation for tremor: spend less, get more. *Brain Stimul* 2018;11:600–606. https://doi.org/10.1016/j.brs.2017.12.015.
16. Peña E, Zhang S, Patriat R et al. Multi-objective particle swarm optimization for postoperative deep brain stimulation targeting of subthalamic nucleus pathways. *J Neural Eng* 2018;15:066020. https://doi.org/10.1088/1741-2552/aae12f.
17. Dembek TA, Reker P, Visser-Vandewalle V et al. Directional DBS increases side-effect thresholds-a prospective, double-blind trial. *Mov Disord* 2017;32:1380–1388. https://doi.org/10.1002/mds.27093.
18. Pollo C, Kaelin-Lang A, Oertel MF et al. Directional deep brain stimulation: an intraoperative double-blind pilot study. *Brain* 2014;137:2015–2026. https://doi.org/10.1093/brain/awu102.
19. Schnitzler A, Mir P, Brodsky M, et al. Directional or omnidirectional Deep Brain Stimulation for Parkinson's disease: results of a prospective blinded-comparison multi-centre clinical study [abstract]. In: *3rd International Brain Stimulation Conference*. Vancouver; 2019.
20. Ten Brinke TR, Odekerken VJJ, Dijk JM, van den Munckhof P, Schuurman PR, de Bie RMA. Directional deep brain stimulation: first experiences in centers across the globe. *Brain Stimul* 2018;11:949–950. https://doi.org/10.1016/j.brs.2018.04.008.
21. Iacono MI, Neufeld E, Akinnagbe E et al. MIDA: a multimodal imaging-based detailed anatomical model of the human head and neck. *PLoS One*. 2015;10:e0124126. https://doi.org/10.1371/journal.pone.0124126.
22. DATABASE » IT'IS Foundation. https://itis.swiss/virtual-population/tissue-properties/database/.
23. Ineichen C, Shepherd NR, Sürücü O. Understanding the effects and adverse reactions of deep brain stimulation: is it time for a paradigm shift toward a focus on Heterogenous biophysical tissue properties instead of electrode design only? *Front Hum Neurosci* 2018;12:468. https://doi.org/10.3389/fnhum.2018.00468.
24. Butson CR, Cooper SE, Henderson JM, McIntyre CC. Patient-specific analysis of the volume of tissue activated during deep brain stimulation. *Neuroimage* 2007;34:661–670. https://doi.org/10.1016/j.neuroimage.2006.09.034.
25. Gunalan K, Chaturvedi A, Howell B et al. Creating and parameterizing patient-specific deep brain stimulation pathway-activation models using the hyperdirect pathway as an example. *PLoS One* 2017;12:e0176132. https://doi.org/10.1371/journal.pone.0176132.
26. Howell B, McIntyre CC. Role of soft-tissue heterogeneity in computational models of deep brain stimulation. *Brain Stimul* 2017;10:46–50. https://doi.org/10.1016/j.brs.2016.09.001.
27. Gunalan K, Howell B, McIntyre CC. Quantifying axonal responses in patient-specific models of subthalamic deep brain stimulation. *Neuroimage* 2018;172:263–277. https://doi.org/10.1016/j.neuroimage.2018.01.015.
28. Schüpbach WMM, Chabardes S, Matthies C et al. Directional leads for deep brain stimulation: opportunities and challenges. *Mov Disord* 2017;32:1371–1375. https://doi.org/10.1002/mds.27096.
29. Grill WM, Thomas Mortimer J. Electrical properties of implant encapsulation tissue. *Ann Biomed Eng* 1994;22:23–33. https://doi.org/10.1007/BF02368219.
30. McIntyre CC, Richardson AG, Grill WM. Modeling the excitability of mammalian nerve fibers: influence of afterpotentials on the recovery cycle. *J Neurophysiol* 2002;87:995–1006. https://doi.org/10.1152/jn.00353.2001.
31. Nambu A, Takada M, Inase M, Tokuno H. Dual somatotopical representations in the primate subthalamic nucleus: evidence for ordered but reversed body-map transformations from the primary motor cortex and the supplementary motor area. *J Neurosci* 1996;16:2671–2683.
32. Parent A, Hazrati LN. Functional anatomy of the basal ganglia. II. The place of subthalamic nucleus and external pallidum in basal ganglia circuitry. *Brain Res Brain Res Rev* 1995;20:128–154.
33. Butson CR, Maks CB, McIntyre CC. Sources and effects of electrode impedance during deep brain stimulation. *Clin Neurophysiol* 2006;117:447–454. https://doi.org/10.1016/j.clinph.2005.10.007.
34. Tass PA, Qin L, Hauptmann C et al. Coordinated reset has sustained aftereffects in Parkinsonian monkeys. *Ann Neurol* 2012;72:816–820. https://doi.org/10.1002/ana.23663.
35. Adamchic I, Hauptmann C, Barnikol UB et al. Coordinated reset neuromodulation for Parkinson's disease: proof-of-concept study. *Mov Disord* 2014;29:1679–1684. https://doi.org/10.1002/mds.25923.
36. Xu W, Miocinovic S, Zhang J, Baker KB, McIntyre CC, Vitek JL. Dissociation of motor symptoms during deep brain stimulation of the subthalamic nucleus in the region of the internal capsule. *Exp Neurol* 2011;228:294–297. https://doi.org/10.1016/j.expneurol.2010.08.007.

SUPPORTING INFORMATION

Additional supporting information may be found online in the supporting information tab for this article.

